

Flare-associated energetic particles in the corona and at 1 AU

K.-L. Klein¹, E.L. Chupp², G. Trotter¹, A. Magun³, P.P. Dunphy², E. Rieger⁴, and S. Urpo⁵

¹ Observatoire de Paris, Section de Meudon, DASOP, CNRS-UMR 8645, F-92195 Meudon, France

² University of New Hampshire, Physics Department and Space Science Center, Durham, NH 03824, USA

³ University of Bern, IAP, Sidlerstrasse 5, CH-3012 Bern, Switzerland

⁴ Max-Planck-Institut für Extraterrestrische Physik, D-85740 Garching bei München, Germany

⁵ Metsähovi Radio Observatory, Metsähovintie 114, FIN-02540 Kylmälä, Finland

Received 17 July 1998 / Accepted 20 April 1999

Abstract. It is widely believed that the longest lasting and most energetic solar energetic particle events (SEPs) observed in interplanetary space result from acceleration by the bow shocks of coronal mass ejections (CMEs). Using gamma-ray, X-ray and radio diagnostics of interacting particles and spaceborne and ground-based detection of ≥ 20 MeV protons at 1 AU during two large events (1989 September 29 and October 19), we demonstrate that time-extended acceleration processes in the low and middle corona, far behind the CME, leave their imprints in the proton intensity time profiles in interplanetary space for one to several hours after the onset of the flare: (1) New increases of ≥ 20 MeV proton fluxes at 1 AU can be traced back to episodes of coronal acceleration. (2) Increasing richness of relativistic protons observed at 1 AU in the course of the SEPs is associated with new coronal particle injection after the impulsive phase. (3) Particle injection sites enabling a rapid access to the well-connected magnetic field line, as required by the SEP time profile, exist in the middle corona even if the nominal $H\alpha$ flare location is far away. These findings suggest that contrary to the prevalent view acceleration processes in the low and middle corona supply both interacting and at least part of the interplanetary particles. The association of the most proton-rich component of the SEPs with delayed low-frequency radio emission is consistent with ionization state studies of SEPs, in that both require acceleration in a tenuous plasma. We conclude that the complexity of the corona provides the ingredients for the acceleration of particles and their injection into a large range of heliocentric angles. The CME may play the role of a trigger or even contribute to the buildup of magnetic stresses in the corona, but its bow shock is not the main accelerator of the high-energy protons.

Key words: Sun: activity – Sun: corona – Sun: flares – Sun: particle emission – Sun: radio radiation

1. Introduction

Since the discovery in 1942 of the so called “solar cosmic rays” and their interpretation as relativistic protons it has been assumed that the processes causing the visible flare have also created the conditions for acceleration of ambient charged particles (cf. Chupp 1996, for a historical review). The increased particle fluxes in interplanetary space following flares were thought to reveal particles escaping from the flare site, and it was expected that a correlation would be found between the yield of interacting particles (producing the X-rays, gamma-rays and neutrons) and the peak particle intensities measured at 1 AU (the solar energetic particle events, SEPs, and the relativistic protons whose signature is detected at the ground, GLEs). However, no convincing correlation was found (Cliver et al. 1989), and doubts arose whether there was a physical link between the energetic particle populations observed at the Sun and near 1 AU. The doubts were substantiated by the finding that ionization states of SEP events detected in situ and longitude distributions of the associated flares display a bimodal distribution (Reames 1990, 1994; Kahler 1992, 1996): “impulsive” events with charge states pointing to acceleration in hot ($\sim 10^7$ K) plasma are seen within a relatively narrow range around the well-connected magnetic field line between the flare site and the detector; particles of “gradual” events, among which are the largest SEPs in terms of proton flux and energy, are accelerated in regions with temperatures $\sim 10^6$ K, could only have traversed small amounts of plasma in order to maintain their low ionization states (Ruffolo 1997), and are associated with flares at any central meridian distance. In contrast to the SEP signatures at 1 AU, no characteristic difference has been found between the interacting ions (Murphy et al. 1991) or the spectra of interacting electrons (Ramaty et al. 1993; Bruggmann et al. 1994) in rapidly and slowly evolving events. This prompted the presently widespread view that impulsive SEPs reveal particles accelerated during the flare, while the gradual SEPs are accelerated in the high corona.

Since gradual SEPs are statistically associated with CMEs and interplanetary shock waves, it is argued (e.g. Kahler et al. 1984; Reames 1990, 1994; Kahler 1992, 1996) that in these events the bulk of ions of any energy is accelerated by the bow shock of the CME while it travels through the high corona

($\geq 5 R_{\odot}$, Kahler 1994), and that acceleration processes in the middle and low corona ($\leq 1 R_{\odot}$, say) do not contribute significantly.

The extended bow shock of a fast CME is an attractive candidate for particle acceleration in the corona: first, it operates in an environment different from the site where most interacting particles revealed by their gamma-ray, hard X-ray and microwave emission are energized, and this might therefore explain the different ionization states in the impulsive and gradual SEP events; second, it could conceivably account for the long duration of gradual SEP events and for the particles' ability to gain access to a large longitudinal range of interplanetary magnetic field lines (Reames et al. 1996). However, the solar corona provides a variety of plausible acceleration mechanisms (e.g. Miller et al. 1997). Furthermore observations show that in various circumstances well-identified shock waves are not the efficient accelerators they were thought to be (Klein et al. 1983, 1988; Kahler 1984; Klein & Trotter 1994), or that their efficiency drops at proton energies between a few MeV and 100 MeV (Sarris & Krimigis 1985; Kallenrode 1993; Ruffolo et al. 1998; Lario et al. 1998). On the other hand, radiative signatures of long-lasting as well as high coronal acceleration and of rapid particle transport are observed when no CME bow shock can be invoked:

- Electron acceleration at altitudes up to several 10^5 km is not only a signature of gradual SEPs, but is also seen during major (Kane et al. 1992) and minor (Klein et al. 1997) flares and in the absence of flares (Lin 1985, 1997; Cliver & Kahler 1991; Krucker et al. 1995).
- Acceleration lasting several hours is evident both for sub-relativistic electrons (type IV radio bursts; e.g. Pick 1986 and references therein) and for relativistic ions (Kanbach et al. 1993; Leikov et al. 1993; Kocharov et al. 1994; Akimov et al. 1996). Time-extended plasma heating during gradual soft X-ray events occurs together with CMEs, but imaging observations show sources and restructuring at heights below $\sim 1 R_{\odot}$ above the photosphere that imply energy conversion far behind the CME (cf. e.g. Klimchuk 1996, and references therein).
- Complex acceleration sites encompassing diverging magnetic field lines (Chupp et al. 1993; Trotter et al. 1994) and particle transport along extended loop structures (Nakajima et al. 1985) grant particles access to a range of heliocentric angles up to several tens of degrees.

In summary, neither long-lasting acceleration nor high coronal acceleration of gradual SEPs imply that shock waves are the only possible or plausible mechanism for accelerating ions and electrons from subrelativistic to relativistic energies. The alternative, acceleration in the magnetically stressed corona at heights below, say, $1 R_{\odot}$ above the photosphere, is viable, provided it occurs in regions sufficiently tenuous to respect the constraints from the observed low ionization states, and that particles have access to a wide range of interplanetary magnetic field lines. In the following, we refer to this height range as the “low and middle corona”. If acceleration in this height range plays a role in SEPs, we expect to see common temporal struc-

tures in the tracers of interacting particles and in proton fluxes detected in interplanetary space.

Here we investigate interacting and interplanetary particles during two major gradual solar flares on 1989 September 29 and October 19 from the same active region. We analyse interacting electrons and protons through radio, hard X-ray and gamma-ray data, showing that the particles are accelerated in, or transported to, different sites in the solar atmosphere. The detailed analysis is given in Sect. 3, and the results relevant to the subsequent discussion of the relationship between coronal acceleration and SEPs are summarized in Sect. 4.1. The temporal and gross spectral evolution of proton fluxes at 1 AU are compared with the time evolution of coronal electron acceleration signatures in the remainder of Sect. 4.

2. Instruments

The Nançay Radioheliograph (NRH; Radioheliograph Group 1989) consists of two orthogonal interferometer arrays, each measuring one-dimensional brightness distributions of the corona. In 1989 the north-south array performed observations at five frequencies (in the two events studied: 164, 237, 327, 408, 435 MHz), and the east-west array observed at 164 MHz. This provides the localization of the centroid and the dimension of the source projected onto the interferometer baselines, i.e. determination of the complete plane-of-the-sky position at 164 MHz, but of only one coordinate at higher frequencies. The accuracy of absolute position measurements is about $0.2'$. The highest time resolution was, respectively, 0.05 and 0.25 s with the east-west and north-south arrays. Spectral identification of the emissions was provided by the spectrographs of Tübingen University in Weissenau (H. Urbarz) and of Paris Observatory in Nançay (M. Poquérusse).

Flux densities at centimetric-to-millimetric wavelengths were observed by the University of Bern polarimeters at 3.1, 5.2, 8.4, 11.8, 19.6, 35 and 50 GHz, with sampling time 0.1 s during the events. The data were calibrated with absolute values of the quiet sun published in the Solar Indices Bulletin (NGDC, Boulder, Colorado). Observed quiet sun fluxes above 15.4 GHz are not available on a regular basis. Values of 700, 2400, and 4500 sfu have been taken for 19.6, 35 and 50 GHz (Croom 1979). These values are independent of solar activity outside flares (S-component) that becomes prominent below 10 GHz. Data of the quiet Sun before the bursts and sky observations were used to calibrate the burst fluxes within an error of approximately $\pm 10\%$, to which errors due to the variation of atmospheric absorption must be added. During the 1989 September 29 event the Sun was mapped by the Metsähovi single dish radio telescope operating at 87 GHz with $1'$ beam size.

High-energy photon observations were made with the Solar Maximum Mission (SMM) Gamma-Ray Spectrometer (GRS; Forrest et al. 1980), and its auxiliary X-ray detectors. The GRS provided flare and background spectra in several energy channels between 14 keV and >100 MeV with time resolutions ranging from 1.024 s to 16.384 s. The primary spectral information

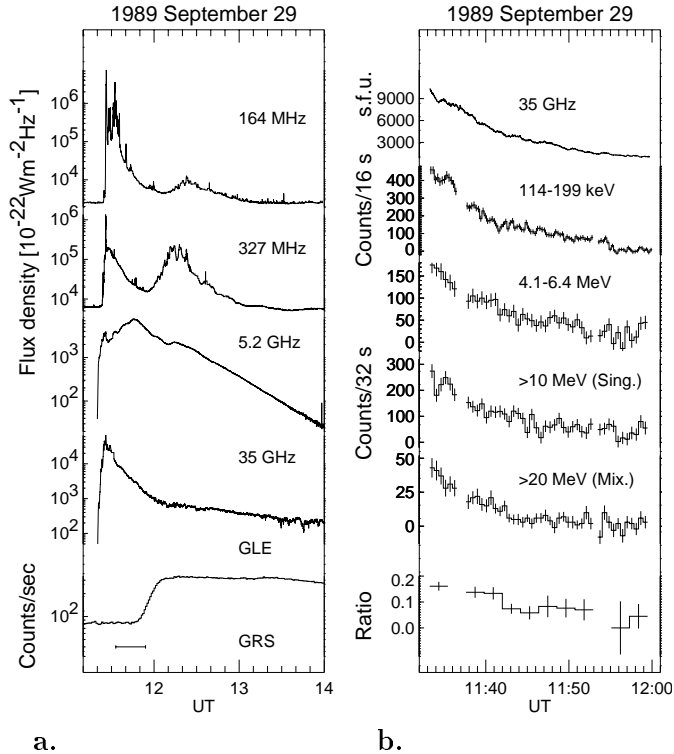


Fig. 1. **a** Time history of the flux density on 1989 September 29 at microwave (Bern) and decimetric-to-metric (Nançay) frequencies and of the energetic protons at 1 AU observed by the Hobart neutron monitor (GLE; energy above 1.1 GeV). The horizontal bar gives the time interval when the Gamma-Ray Spectrometer (GRS) on SMM was observing. **b** Time history of the count rates for several X and gamma-ray energy bands observed by GRS, and of the 35 GHz flux density. The meaning of the “mixed” and “singles” counts and their ratio (bottom panel) is explained in App. A.1.

is the “main channel” data in the range $\sim (0.3\text{--}10)$ MeV with a time resolution of 16.384 s.

Proton fluxes at 1 AU were measured with the GSFC charged particle instrument on IMP-8 (R.E. McGuire), the GOES particle detectors (NOAA; data provided by H. Sauer & R. Vainio) and the worldwide network of neutron monitors whose data were made available through the data base at Phillips Laboratory (L.C. Gentile).

$H\alpha$ flare images were available through the daily observations at Haute Provence Observatory (I. Soru-Escaut, Z. Mouradian), Kanzelhöhe Observatory (A. Schroll), Sacramento Peak (D. Neidig) and Wrocław (I. Garczynska, B. Rompolt). SMM coronagraph observations have been provided courtesy of the High Altitude Observatory. Meudon daily spectroheliograms in $H\alpha$ and Ca II were also used.

3. Interacting particles and coronal structures

Several large particle events, detected by spacecraft and on ground, were produced in association with one active region in autumn 1989: an event on September 29 occurred one day after the region crossed the western limb, and three others, on

October 19, 22 and 24, when the region was again on the disk. In this section we discuss the properties of the interacting particles in the solar atmosphere and their source configuration during the September 29 and October 19 events. The SEP and GLE particle observations for both events will be discussed together in Sect. 4.

3.1. 1989 September 29

An X9.8/1B flare occurred at 1141 UT, together with a coronal mass ejection (CME) observed by the Coronagraph/Polarimeter aboard SMM. The associated particle event provided the highest energy (~ 25 GeV) protons ever observed at the Earth, was the first event recorded by an underground muon telescope, and one of the largest GLEs recorded by a neutron monitor (Swinson & Shea 1990).

The time histories of the whole-Sun radio, X and gamma-ray emissions are plotted in Fig. 1. Radio emission from millimetric to metric waves rises between 1120 and 1125 UT. There is a common phase of bright emission at all frequencies, followed by a monotonic decay after 1130 UT at the highest frequencies, but by renewed rises at centimetric-to-metric wavelengths. The SMM GRS was in low power due to a radiation belt passage until 1133:32 UT, so there is no overlap with the initial flare emissions at soft X-ray and radio wavelengths. Intense emission was observed in all GRS channels until 1154 UT when SMM entered solar eclipse. Background-subtracted time histories (Fig. 1b) display a decay similar to the high-frequency microwaves and the decimeter-meter-wave radio emission.

3.1.1. Large-scale disturbance and radio emission in the corona

Fig. 2 shows the time evolution of the optical emission in $H\alpha$ (left column) and coronal white light (2nd column), and of the decimetric to metric radio sources.

No $H\alpha$ signature is detected during the early appearance of the CME above the south-western limb (Fig. 2, upper row). During the next coronagraph image (central row) the CME has travelled to $\geq 2 R_{\odot}$ above the photosphere. Underneath the tops of post-flare loops become visible in $H\alpha$ from a site behind the limb. While the CME leaves the field of view, the post flare loops grow continuously (bottom row) until around 1900 UT (Sacramento Peak). They still exist at 2315 UT (Fig. 2 of Swinson & Shea 1990).

The location of the $H\alpha$ loops points to a flare in active region NOAA 5698. Its main sunspot is situated approximately 7° to 10° beyond the west limb at 1100 UT. The extrapolation of flares reported for this active region in *Quarterly Bulletin of Solar Activity* (QBSA Vol. 31) between September 22 and 28 leads to a similar value (cf. also Vestrand & Forrest 1993). This implies an occultation height between 5000 and 10000 km.

Decimetric-to-metric radio sources spread from a site above AR 5698 to the whole range spanned by the CME. The evolution is described in the two right-hand columns of Fig. 2. The radio source configuration is incompletely determined at frequencies

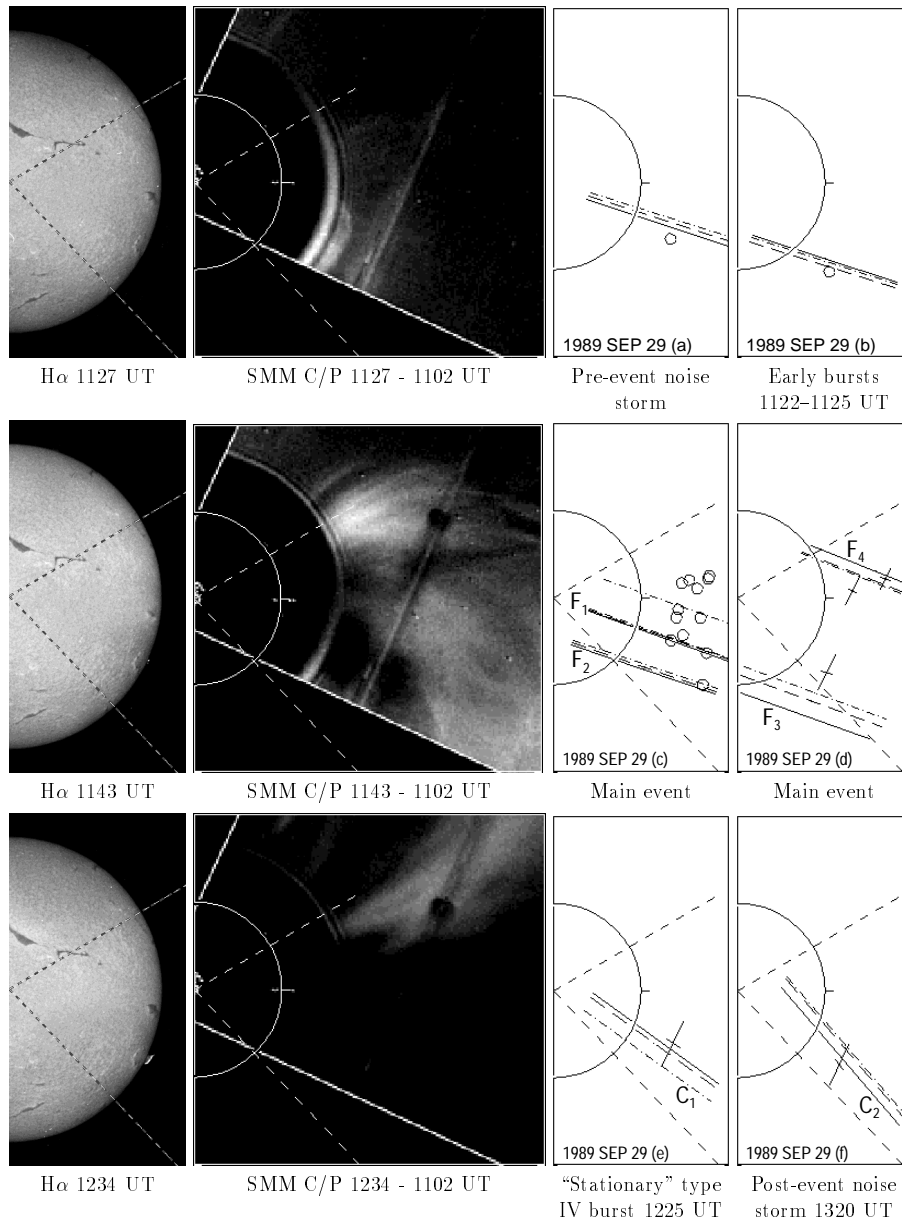


Fig. 2. Time evolution of the 1989 September 29 event: $H\alpha$ (first column; *Observatoire de Haute Provence*, I. Soru-Escaut, Z. Mouradian), coronagraphic difference images (second column, SMM C/P, *High Altitude Observatory*), decimetric and metric radio sources (third and fourth columns; *Nançay Radioheliograph*). Small circles designate the centroids, crosses the centroids and dimensions measured with the two one-dimensional arrays at 164 MHz. Parallel straight lines give the loci of the source centroids at 237 (solid), 327 (long dashes) and 408 or 435 MHz (dashed-dotted). The radial dashed lines delimit the span of the CME (Burkpile & St.Cyr 1993). The north-westward inclined line and dark spot in the coronagraph images are instrumental artifacts.

above 164 MHz. But using the fact that for plasma emission the source height increases with decreasing frequency, different source complexes can be identified and compared with the $H\alpha$ and coronagraphic observations (Fig. 2a–f):

- (a) Weak noise storm emission, existing prior to the flare, brightens at 1122:45 UT. The farther south the sources are, the lower their frequency.
- (b) Sporadic bursts which are too weak to be identified in the Weissenau dynamic spectrum come from a source slightly south of the noise storm, probably from a different coronal structure, since their sources do not display the systematic ordering from high to low frequencies. Both the noise storm and these bursts appear to be emitted in coronal structures that extend south-westward from AR 5698 behind the limb, in a region where the CME is first seen at 1127 UT. Isolated weak bursts had been observed by the NRH since 1050 UT within this area, especially at 237 and 327 MHz.
- (c) The main event starts near 1125:50 UT at decimetric-to-dekametric wavelengths. It consists of a superposition of broadband emission and fast drift bursts. While metric radio sources (circles) are scattered over a large domain, sources at higher frequencies cluster in two principal groups (F_1 , F_2) under the span of the early CME.
- (d) As the radio event proceeds through its phase of brightest emission, sources spread both southward (F_3) and northward (F_4), as does the CME.
- (e) The fading of the main event after 1145 UT (see also Fig. 1) is followed by a new rise, over a broad band from a few GHz (see below) to metric wavelengths, between 12 and 13 UT. The brightest source at decimetric-to-metric wavelengths (C_1 , stationary type IV burst) extends north-westward from the vicinity of the southern footpoint of the CME.
- (f) Noise storm emission persists at C_2 until 14 UT at decimetric wavelengths, until after the end of the NRH observa-

tions (1520 UT) in meter waves. The sources extend southwestward from AR 5698, similar to the pre-event noise storm (Fig. 2a).

The radio source configuration implies multiple magnetic structures that are anchored in different regions of the photosphere, including the active region where the flare occurs and the projected positions of the legs of the CME, covering a latitude range of $\sim 80^\circ$. Prior to and after the brightest flare emission radio emitting electrons are related to the flaring active region south of the equator. During the brightest radio emission, radio sources underlie the whole span of the CME. The front of the CME is inferred to be at a height of $6 R_\odot$ at 12 UT, given the starting time and speed reported by Kahler (1994).

3.1.2. Energetic electrons in the low corona: microwaves

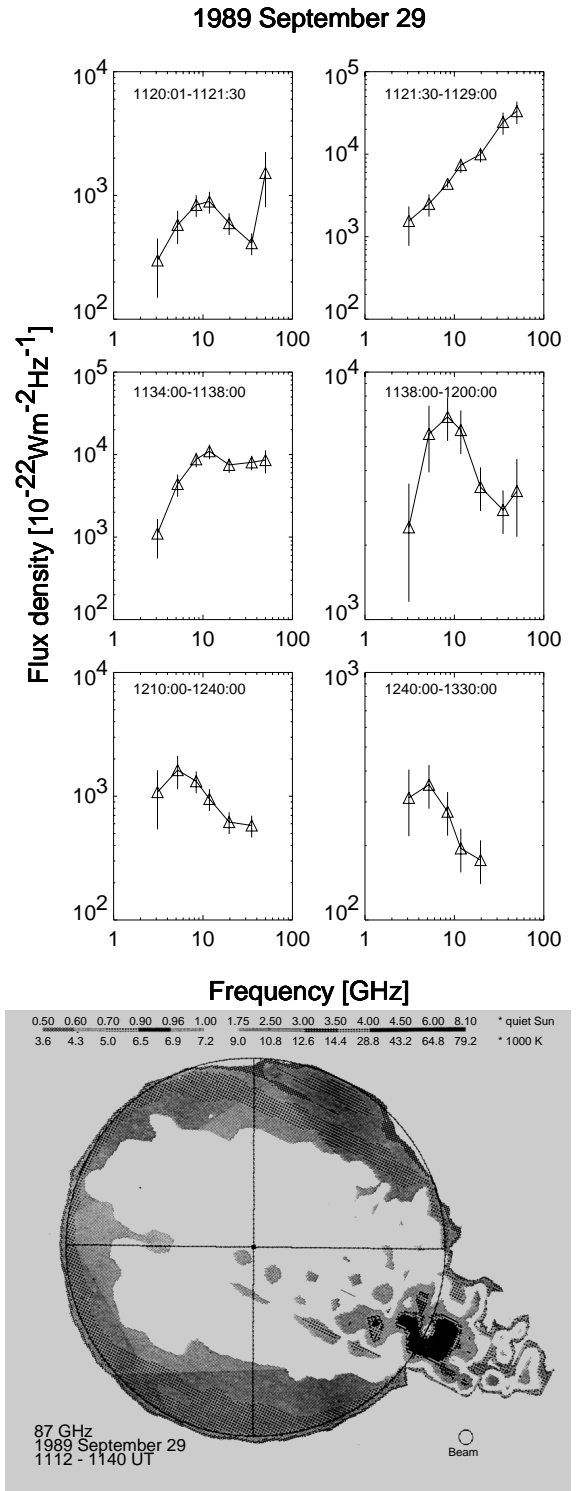
Although the $H\alpha$ signature of the flare occurs in the occulted active region, analysis of microwave and gamma-ray data shows that energetic electrons and ions must also interact on the disk.

The microwave emission produced by mildly relativistic electrons displays a distinctly different evolution at different frequencies (Figs. 1, 3a):

- Emission with a strong millimetric component (turnover frequency ≥ 50 GHz) dominates during the main dm-m event (1120–1138 UT). Subsequently the emission above ~ 35 GHz decays monotonically, as illustrated by the 35 GHz time history in Fig. 1a.
- The brightest peak at centimetric waves is observed from 1135 to 1200 UT (e.g. 5.2 GHz, Fig. 1). It has neither a millimetric nor a metric counterpart (low-frequency cutoff ~ 600 MHz, cf. the flux density time histories in Bhatnagar et al. 1996, Fig. 1b).
- After ~ 12 UT fluctuations are superposed on the decaying emission from the centimetric peak. They are associated with the stationary type IV continuum at dm-m- λ . The emission has no counterpart in the millimeter range (e.g. 35 GHz in Fig. 1a).

These observations imply that at least two source regions contribute to the microwave emission. The deficiency of both metric and millimetric emission during the main peak around 1150 UT at e.g. 5 GHz is expected when energetic electrons radiate in active region loops which do not reach the higher corona ($> 10^5$ km, say), and whose footpoints are occulted (e.g. Kai et al. 1986). This is consistent with emission from a loop anchored in the occulted active region. On the other hand, gyrosynchrotron spectra with maxima at millimetric wavelengths (1120–1138 UT) require that self absorption, Razin suppression or free-free absorption in the ambient plasma be effective up to unusually high frequencies, implying strong magnetic fields or high ambient density ($B \geq 10^3$ G, $n_e > 10^{11}$ cm $^{-3}$; e.g. Klein 1987). These parameters are unlikely at the heights of the post-flare loops and indicate a source on the visible disk.

The 87 GHz map taken at Metsähovi during the event confirms this conclusion (Fig. 3b): emission comes from above the



a.

b.

Fig. 3. a The microwave spectrum for six intervals of time during the 1989 September 29 event. Vertical error bars give the uncertainty of the absolute flux density calibration at frequencies up to 35 GHz, and the combined errors of absolute calibration and fluctuations of atmospheric absorption at 50 GHz. **b** Map of the Sun at 87 GHz during the 1989 September 29 event (Metsähovi Radio Observatory). The map was obtained by scanning the Sun in right ascension. One scan requires 54 s, the scan across the brightest source was taken at 1126 UT. Sidelobes have been subtracted. Dark shading outside the polar regions means bright emission.

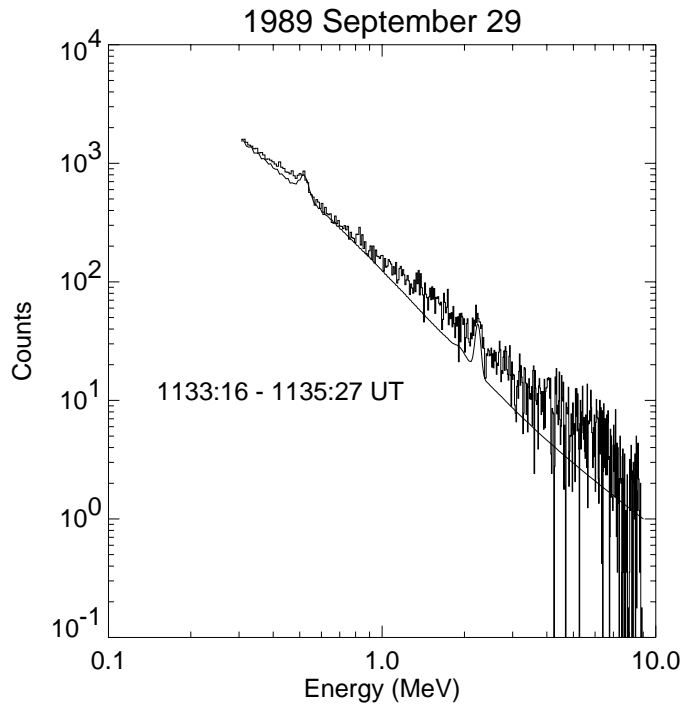


Fig. 4. The GRS main channel energy loss spectrum during part of the decay phase of the 1989 September 29 event. The continuous line shows a model fit to the data using a power law photon continuum, a line at 0.511 MeV, and a line at 2.22 MeV. The prompt line spectrum was omitted from the fit so that the net contribution of the lines in the ranges (1.1–1.8) MeV and (4.1–7.6) MeV could be determined.

limb, i.e. the vicinity of the $H\alpha$ loops, but extends onto the disk. The map is obtained by scanning the Sun and is therefore a distorted image of the source configuration, due to the combined effect of scanning and time evolution of the radio source. This creates e.g. the aligned bright patches (dark shading) on the disk during the scan through the brightest source. However, the brightest source itself is large and bridges the limb, and this cannot be simulated by a time-varying signal from a source above the limb received through the sidelobes.

3.1.3. Energetic ions in the low atmosphere: gamma rays

The ratio of “mixed” to “singles” counts plotted at the bottom of Fig. 1b is a measure of the relative contribution of photons and of <500 MeV neutrons to the count rate of the high energy monitor (HEM; cf. App. A.1.). Its value and evolution are similar during the partially occulted event of September 29 and the disk event on October 19, showing the increasing contribution of directly detected neutrons to the detected signal.

The gamma-ray line emission gives further arguments for a source on the disk:

- The most striking feature in the GRS spectrum (Fig. 4), which displays both strong continuum and narrow line emission, is the significant peak nominally at ~ 2.223 MeV produced by photospheric neutron capture. For a neutron interaction region well behind the limb the line’s intensity would

be attenuated by a factor of 100 or more from the intensity of the source if it were at disk center.

- A thin target interaction model, which would be required in order to explain prompt gamma-ray line emission from a loop anchored in the occulted active region, can be ruled out by a study of R , the ratio of (1.1–1.8) MeV and (4.1–7.6) MeV nuclear gamma-ray line fluences (not to be confused with the ratio in Fig. 1b; cf. App. A.2.). In the present event R has an average value of 1.3 and varies progressively from ~ 1.4 (1133 UT) to ~ 1.1 (1153 UT). Only a thick target interaction region is consistent with these values.

Based on the interpretation of the R values and the microwave evidence for a visible disk source, we conclude that the observed 2.223 MeV and (4.1–6.4) MeV emissions in the 1989 September 29 flare are predominantly from photospheric and chromospheric sources, respectively, on the visible disk, presumably near the limb. Vestrand & Forrest (1993, 1994) attributed the nuclear gamma-ray line production to the backward precipitation of ions, accelerated by a CME driven shock wave, onto a wide expanse of the lower corona/chromosphere. However the CME acceleration model cannot be generally valid since the 1991 June 1 flare, certainly one of the strongest gamma-ray line flares ever observed (Ramaty et al. 1997), was also well behind the limb with its main component of emission obscured, but no neutron–proton capture line was observed, and the gamma-ray line emission was produced in a thin target coronal source (Barat et al. 1994; Trotter et al. 1996; Ramaty et al. 1997). Particle transport from the occulted active region along large-scale magnetic loops is a plausible alternative process, as shown by Vilmer et al. (1999) for another large X/gamma-ray event.

3.2. 1989 October 19

An X13/4B event occurred in NOAA active region 5747 slightly east of central meridian (nominal location in SGD : S25° E09°). Backward extrapolation of the sites of $H\alpha$ flares from this region (QBSA vol. 31) to the time of the 1989 September 29 event leads to S27° W103°. This is close to the extrapolated position of S26° W97° for all flares from AR 5698 between 1989 September 22 and 28. Therefore, we deal with two flares from the same active region. The October 19 event produced intense electromagnetic emissions from the radio to the gamma-ray domains, and a major GLE caused by protons accelerated to energies greater than 4.5 GeV.

The time history of radio, hard X-ray and gamma-ray emissions is plotted in Fig. 5. As during the September 29 event, the initial impulsive phase is followed by a monotonic decay at millimetric frequencies and long-lasting post-impulsive electron acceleration revealed by prolonged emission from centimetric to metric waves. The SMM was occulted by the Earth until ~ 15 minutes after the start of the microwave burst. Fig. 5b shows background-subtracted GRS time histories in several energy channels from hard X-rays through the nuclear line region to above 10 MeV. While the onset of the event is unknown, the observed peak rate in the > 10 MeV band occurs at nearly the

same time as the 50 GHz peak, and the observed decay rate in the (4.1–6.4) MeV band is similar to those at high-frequency microwaves. This confirms the similarity between gamma-ray and microwave time profiles mentioned before.

3.2.1. Flares, active regions and radio emission in the corona

The active region configuration is shown at the top of Fig. 6. Observations at Wroclaw ($H\alpha$ line center) show a brightening of the ribbon between the spots in AR 5747 that is already visible in Fig. 6 (top right) before the major flare. An arcade of post-flare loops, spanning about 20° in heliographic longitude between AR 5747 and 5744, developed during nine hours, while the soft X-ray event decayed over more than seven hours (*SGD* 548-II).

The SMM coronagraph was not operating before 1603 UT (Burkepile & St.Cyr 1993). However, a Sudden Commencement on October 20 is likely associated with this flare (Cliver et al. 1990). This and the long soft X-ray duration make the occurrence of a CME in association with the flare most likely.

The radio source configuration is in many respects similar to September 29:

- Sporadic initial type III bursts (frequencies below 200 MHz) occur above the flaring active region (Fig. 6b).
- During the phase of brightest emission radio sources spread over a broad range of heliocentric angles. Decimetric-to-metric type III bursts (Fig. 6c) are associated with several sources whose ordering as a function of frequency argues for electron injection into magnetic structures that spread both south-eastward (F_1) and westward (F_2) from the active region. Continuum emission then comes from two source complexes (Fig. 6d). One of them (F_3 , at frequencies above 200 MHz) is consistent with a loop system above AR 5747, while the second one (F_4 , at 164 and 237 MHz, distinguished after 1251:20 UT) lies in the western hemisphere, above active region NOAA 5740 (S17W31).
- While the continuum persists at decimetric wavelengths, type II emission is observed below 250 MHz from high above the south-eastern limb (Fig. 6e).
- Although the flux density decreases after 1300 UT, broadband emission from microwave frequencies to meter waves persists without interruption until the end of the NRH observations at 1530 UT (Fig. 5). At dm-m-waves the source is located above AR 5747 (Fig. 6f). A new event occurs at decimetric wavelengths near 1445 UT. The dynamic spectrum shows various types of fast-drift bursts, including ordinary and reverse-drift type III bursts (due to upward and downward propagating electron beams).

The observations of source F_4 (Fig. 6d) indicate a magnetic structure anchored in AR 5740, at a heliocentric distance of 38° from AR 5747 where the $H\alpha$ flare is going on. Although no $H\alpha$ flare is reported in AR 5740 (*SGD* 548-II), pictures taken every 4 minutes at the Kanzelhöhe Observatory show a bright point at 1250 UT in the north-eastern outskirts of AR 5740 which is not there either before or afterwards (Fig. 7). This is another

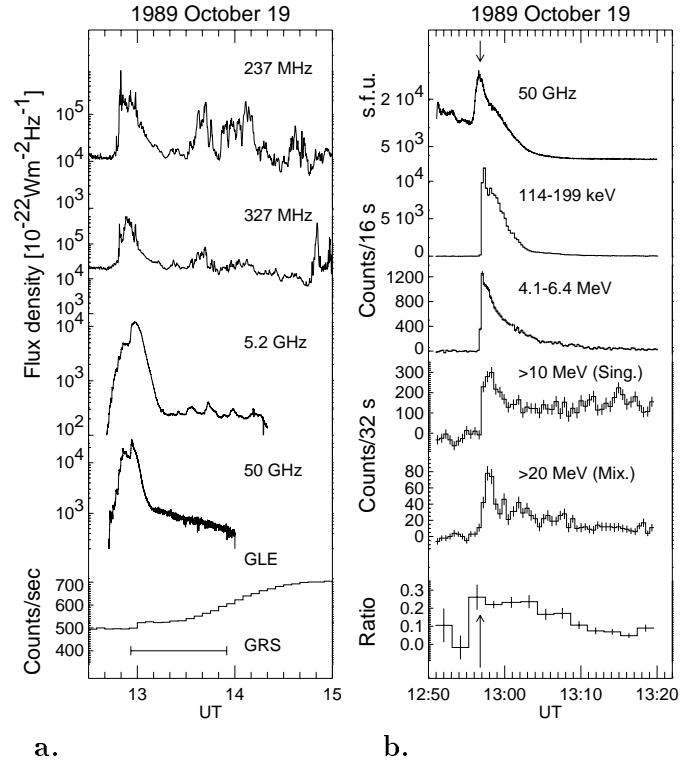


Fig. 5. **a** Time history of the radio flux density and neutron monitor signal on 1989 October 19. The horizontal bar gives the time interval where SMM/GRS was observing. **b** Time history of the count rates at X-rays and gamma-rays. The vertical arrows at the top and bottom indicate sunrise at SMM.

hint that energy is transported to, or released in AR 5740. Due to the strong radio emission from the eastern sources it is not possible to decide whether the western continuum already exists at 1250 UT or not.

3.2.2. Energetic electrons in the low corona: microwaves

As on September 29, the microwave spectrum has two components (Fig. 5):

- Before 1248 UT, while the emission is still weak, the spectrum has a turnover between 11.8 and 19.6 GHz.
- After 1248, that is during the main emission at all frequencies and its decay, the microwave spectrum comprises also a strong millimetric component, which dominates during the decay phase of the main event.
- Low-frequency fluctuations after the decay of the main event show the persistence of electron acceleration over several hours, accompanying decimetric-metric radio emission (e.g. 5.2 GHz in Fig. 5; cf. also *SGD* 543-I for a lower microwave frequency).

3.2.3. Energetic ions in the low atmosphere: gamma rays

Comparison with the September 29 event shows the following (cf. Appendix A):

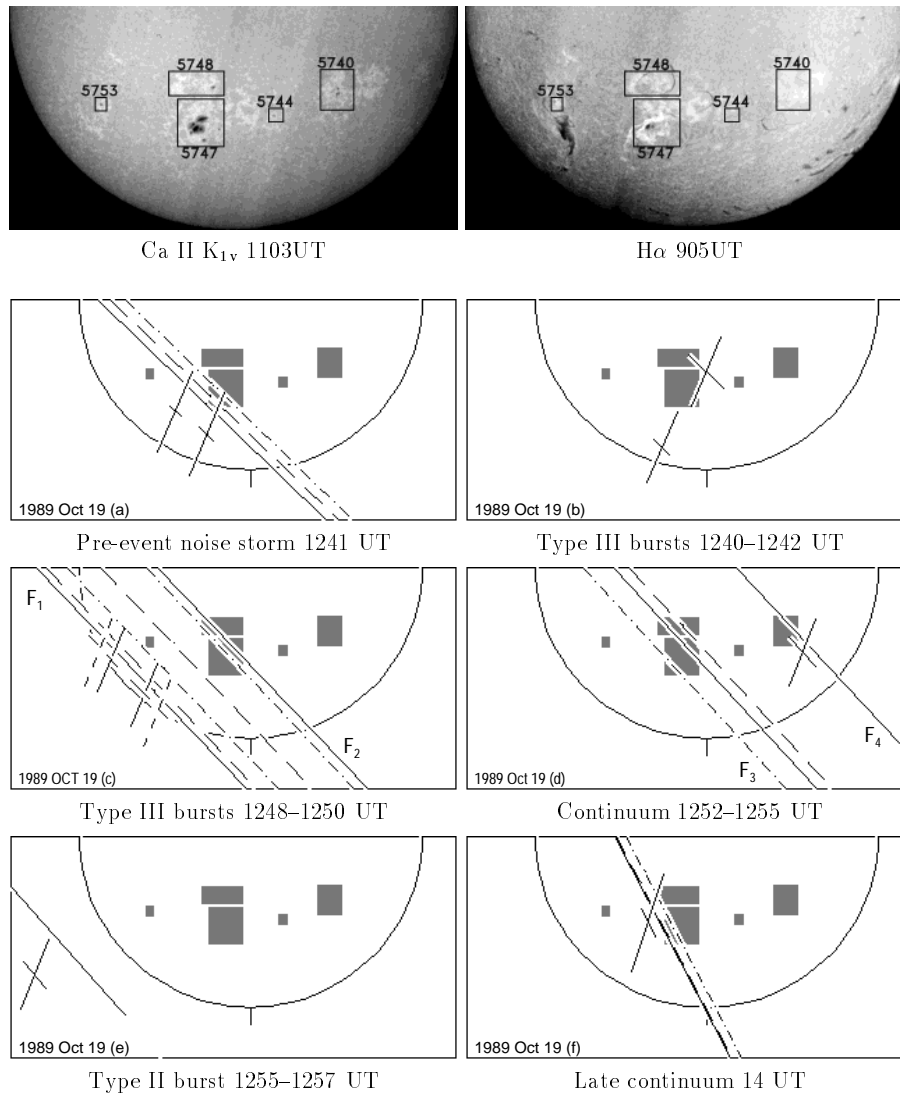


Fig. 6. Pre-event Ca II wing and H α images (Meudon Observatory; upper panel), and decimetric and metric radio sources (three lower panels) during the 1989 October 19 event. Crosses designate the centroids and dimensions measured with the two one-dimensional arrays of the NRH at 164 MHz. Straight lines give the loci of the source centroids at 237 (solid), 327 (long dashes) and 408 or 435 MHz (dashed-dotted). The positions are inferred from data integrated over 10 s.

- The time evolutions of the HEM “mixed” to “singles” events are comparable.
- The 2.223 MeV line (Fig. 8) is more pronounced on October 19, because the flare occurred near central meridian.
- The ratio of (1.1–1.8) MeV and (4.1–7.6) MeV nuclear gamma-ray line fluences and its variation are similar to September 29. These values of the ratio are consistent with a thick target interaction geometry, which is expected for a flare well on the disk.

The observations show that pion-producing protons or relativistic electrons (or both) still interact after the main event. This is evident on October 19, where the count rate above 20 MeV (mixed channel) is still well above background when SMM enters eclipse. The case is not so clear on September 29, but there most of the high-energy emission may have been occulted.

In conclusion, microwave and gamma-ray spectral signatures of the partially occulted event on September 29 and of the disk center flare on October 19 are similar. This reinforces our conclusion that the occulted event actually comprises interaction regions on the visible disk and, more generally, that

energetic electrons and ions interact in several different regions of the low corona, chromosphere and photosphere.

4. Energetic protons at 1 AU

4.1. Interacting particles and the history of coronal acceleration

The combined analysis of broadband radio, gamma-ray and hard X-ray data in the previous section has shown basically two phases during both events:

- The impulsive (main) phase with emissions over the whole range from gamma-rays to metric radio waves. During this phase low-frequency radio sources gradually spread out over a large range of heliocentric angles, and show either that electrons are efficiently transported in the corona over increasingly large distances or that particles are accelerated at widely separated places. While the imaging observations refer to suprathermal electrons, the gamma-ray analysis shows that energetic ions also interact in different regions, at least during the September 29 event.

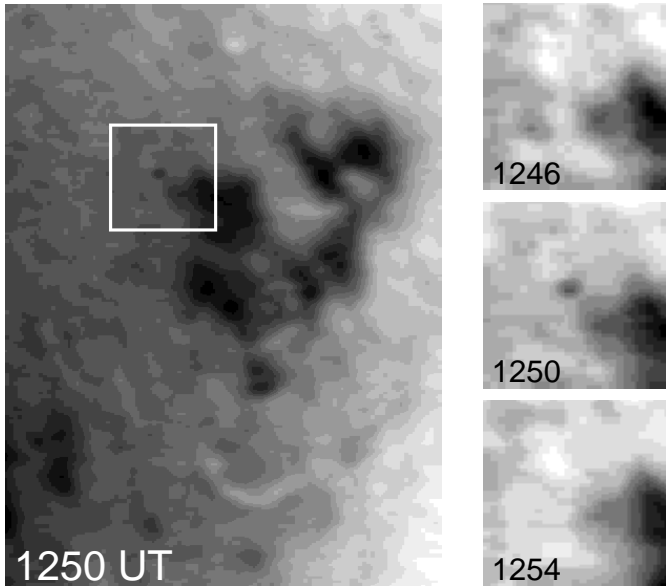


Fig. 7. $H\alpha$ line centre observations on 1989 October 19 of AR 5740 in the western hemisphere (Kanzelhöhe Observatory, Graz University, A. Schroll). Solar north is at the top, east on the left, dark shading means bright emission. The whole active region is shown in the picture on the left, three successive images of its north-eastern outskirts (as delimited by the square in the left figure) are plotted on the right. Note the appearance of a bright point in the 1250 UT image.

- The post-impulsive phase with emission extending mainly from decimetric to metric waves. The post-impulsive radio emission comes from the vicinity of the active region where the main $H\alpha$ emission is observed, and is accompanied by the formation and rise of post-flare loops.

This sequence is typical for long-lasting events (cf. Trotter 1986), and the wide spread of radio sources underneath the CME has been reported elsewhere (e.g. Maia et al. 1999). The restriction to lower radio frequencies in the late phase of the events demonstrates emission from a more dilute plasma than previously. This emission comes from electrons of some tens to a few hundreds of keV. Since such electrons have collisional lifetimes in coronal structures that range from a few to at most several tens of seconds, the long-lasting radio emission is a tracer of time-extended electron acceleration. The complex source configuration and extended duration of particle acceleration in the low and middle corona suggest that energetic particles should have access to interplanetary space from different coronal sites and for an extended duration.

4.2. Observations

The time histories of energetic protons as observed by neutron monitors on 1989 September 29 and October 19 are plotted in Figs. 1a and 5a. Both events have long duration and display the low ionization states of Fe that are typical of gradual particle events (Tylka et al. 1995). Both events display temporal structures, besides the generally observed monotonic rise and fall. We give a short description of the events and then attempt to

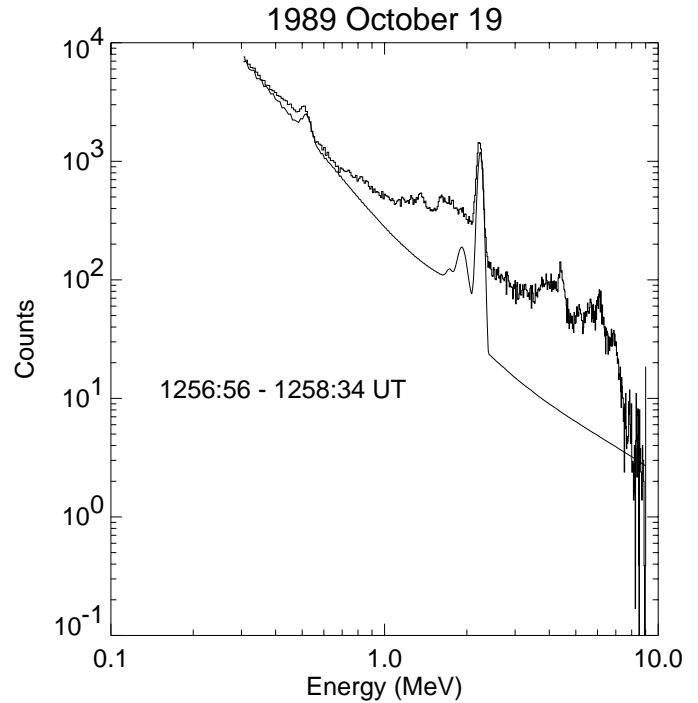


Fig. 8. The GRS main channel spectrum during the decay phase of the 1989 October 19 event (cf. caption of Fig. 4)

connect these time structures to the evolution of coronal acceleration discussed above.

The 1989 September 29 event (Fig. 1) has been extensively studied (Swinson & Shea 1990; Smart et al. 1991; Duldig et al. 1993; Stoker 1994; Torsti et al. 1994; de Koning & Bland 1995; de Koning & Mathews 1995; Mirochnichenko et al. 1997; Tylka et al. 1995, 1997). The neutron monitor data show two maxima between 1200 and 1230 UT and 1315 and 1410 UT, respectively. Detectors with high cutoff rigidity see only the peak 1200–1230, and a subsequent slow monotonic decrease (Swinson & Shea 1990; Smart et al. 1991). While the 1200–1230 UT peak displays a pronounced anisotropy, revealing particles streaming away from the Sun at small pitch angles, the second one is more isotropic and contains particles of solar origin which arrive at the Earth from the anti-sunward direction (Duldig et al. 1993; de Koning & Bland 1995; de Koning & Mathews 1995; Mirochnichenko et al. 1997). Therefore the second peak is probably not the signature of a new particle injection.

The energetic particle event on 1989 October 19 (Fig. 5) has been discussed by Bieber & Evenson (1991), Shea et al. (1991), Reeves et al. (1992), Belian et al. (1992), Stoker et al. (1995) and Anttila et al. (1998). Most neutron monitors observe the count rate to slowly rise after ~ 1330 UT and to level off after ~ 1500 UT. This is usual for events associated with flares east of central meridian. At some neutron monitors this gradual rise is preceded by a short (≤ 30 min) minor peak starting 13 UT (maximum ~ 1315 UT) whose rapid rise and pronounced anisotropy are unusual during flares far from the well-connected interplanetary field line in the western hemisphere.

4.3. Comparison with coronal electron acceleration

In order to identify the time when particles observed in interplanetary space were released, one usually extrapolates the onset of a particle event back to the Sun, employing a suitably averaged propagation speed for each detector channel and a plausible path length along the interplanetary magnetic field (cf., e.g., Kahler 1994; Debrunner et al. 1997). The method works well for the first onset of the particle event, but is uncertain in later phases, when new enhancements are superposed upon a high and variable flux. In order to circumvent this problem, we start with the radio time profiles as the presumed tracers of coronal acceleration processes and calculate when the protons are expected to arrive at 1 AU. We do this assuming that the particles get rapid access to the well-connected interplanetary field line and freely stream along it. In reality the access will be rapid only for particles accelerated in, or rapidly transported to, the western hemisphere, while the others will have to undergo diffusion (cf. e.g. review by Kunow et al. 1991). The actual time profile at 1 AU will therefore be more or less smeared-out with respect to the results of our calculations, depending on how far from the well-connected field line the particles were injected. However, the free-streaming calculations predict the earliest possible onset and the minimum duration of each flux enhancement related with coronal injection. The formulae used for the calculations are discussed in Appendix B.

We emphasize that a basic assumption of this approach is that protons are accelerated with the same time profile as the radio emitting electrons. The close relationship between electron and proton acceleration in the corona is supported by gamma-ray and hard X-ray observations of electrons and protons interacting in the solar atmosphere (Sect. 3; see also Chupp et al. 1993; Kocharov et al. 1994; Trotter et al. 1994; Debrunner et al. 1997). We also refer to Kallenrode & Wibberenz (1991) for examples illustrating the similar time profiles of coronal radio emission and particle fluxes measured at 0.3 to 0.4 AU.

4.4. Results

Figs. 9 and 10 display the observed time histories of proton fluxes in different energy ranges (solid line) and those of the free-streaming calculations using different radio time profiles (dashed line). In these calculations the protons are assumed to be injected with power law index $\delta = 3$ and to travel a distance 1.3 AU through interplanetary space. The results do not change qualitatively for steeper spectra ($\delta = 4, 5$) and longer paths along the magnetic field (≤ 1.7 AU). As expected, the observed time profiles are much smoother than those computed in the free-streaming model. However, we see that most increases in the observed time profile of the protons occur at times when protons are expected to arrive from coronal acceleration regions. There are significant differences depending on which radio frequency is used as the tracer of particle acceleration. We recall (cf. Sect. 3) that injection functions derived from the highest radio frequencies emphasize particle injections in the low corona, below a few 10^4 km above the photosphere, say. Lower frequen-

cies are sensitive to particles that get access to, or are accelerated in, the middle corona, at typical heights of a few 10^5 km for metric wavelengths. We discuss the comparison of computed and observed features separately for the two events.

On 1989 September 29, the 20–80 MeV protons (top panel in Fig. 9) rise near the predicted time of arrival of particles accelerated during the impulsive flare phase. The coronal signature of this injection shows up at all radio frequencies. This proton population has a steep spectrum, since the detectors of protons above 100 MeV (middle and bottom panel) show no response. The subsequent evolution is markedly different for different height ranges of the tracer of coronal particle injection. The high frequency microwaves do not predict the new rise in the 20–80 MeV range near 1230 UT, and the event onset at relativistic energies near 1150 UT. On the other hand, the relativistic event rises so rapidly that its delayed onset cannot be due to interplanetary propagation, but implies a delayed acceleration of the particles with respect to the impulsive flare. This rise can be traced back to coronal particle injection visible from decimetric to metric waves, as illustrated by the second column in Fig. 9, where only the flux density of the stationary type IV (IVS) continuum has been used as injection function. The one-dimensional imaging observations did not provide an unambiguous separation of the time histories of the impulsive emission and of the stationary type IV burst. Therefore the onset of the type IV emission and the decay of the impulsive emission were fitted to exponentials, and the impulsive part was subtracted from the whole Sun flux density. With this injection function the predicted and observed onsets of the relativistic proton event coincide.

The new rise of the proton fluxes starting near 1320 UT at all energies cannot be traced back to coronal acceleration. As discussed in Sect. 4.2, this rise is not necessarily due to new particle acceleration. We cannot decide whether the prolonged particle flux enhancement is exclusively due to interplanetary propagation or whether shock acceleration also contributes. Given the speed of the CME, this would occur at heliocentric distances $> 18 R_{\odot}$. In any case, during the first two hours (until ~ 1320 UT) the proton profile at 1 AU carries signatures of acceleration at coronal altitudes below $1 R_{\odot}$ above the photosphere. The relativistic particle event starts to fade at 1330 UT.

The 1989 October 19 SEP has also two components (Fig. 10). The unusually fast early rise of the relativistic proton fluxes near 13 UT occurs shortly after the predicted arrival of freely streaming protons injected during the impulsive flare phase. The rapidity of the rise is consistent with the injection of energetic particles in the western solar hemisphere suggested by the radio data. There is no need to resort to the ad-hoc assumption that the protons arriving at the Earth result from the decay of primary neutrons, as suggested by Shea et al. (1991) who used this hypothesis to reconcile the rapid rise of the neutron monitor signal with injection near the nominal site of the H α flare. The most intense part of the proton event rises much more slowly, in association with new injections at greater coronal altitudes, which have no counterpart in the high-frequency (e.g. 50 GHz) microwave emission. The slowness of this second

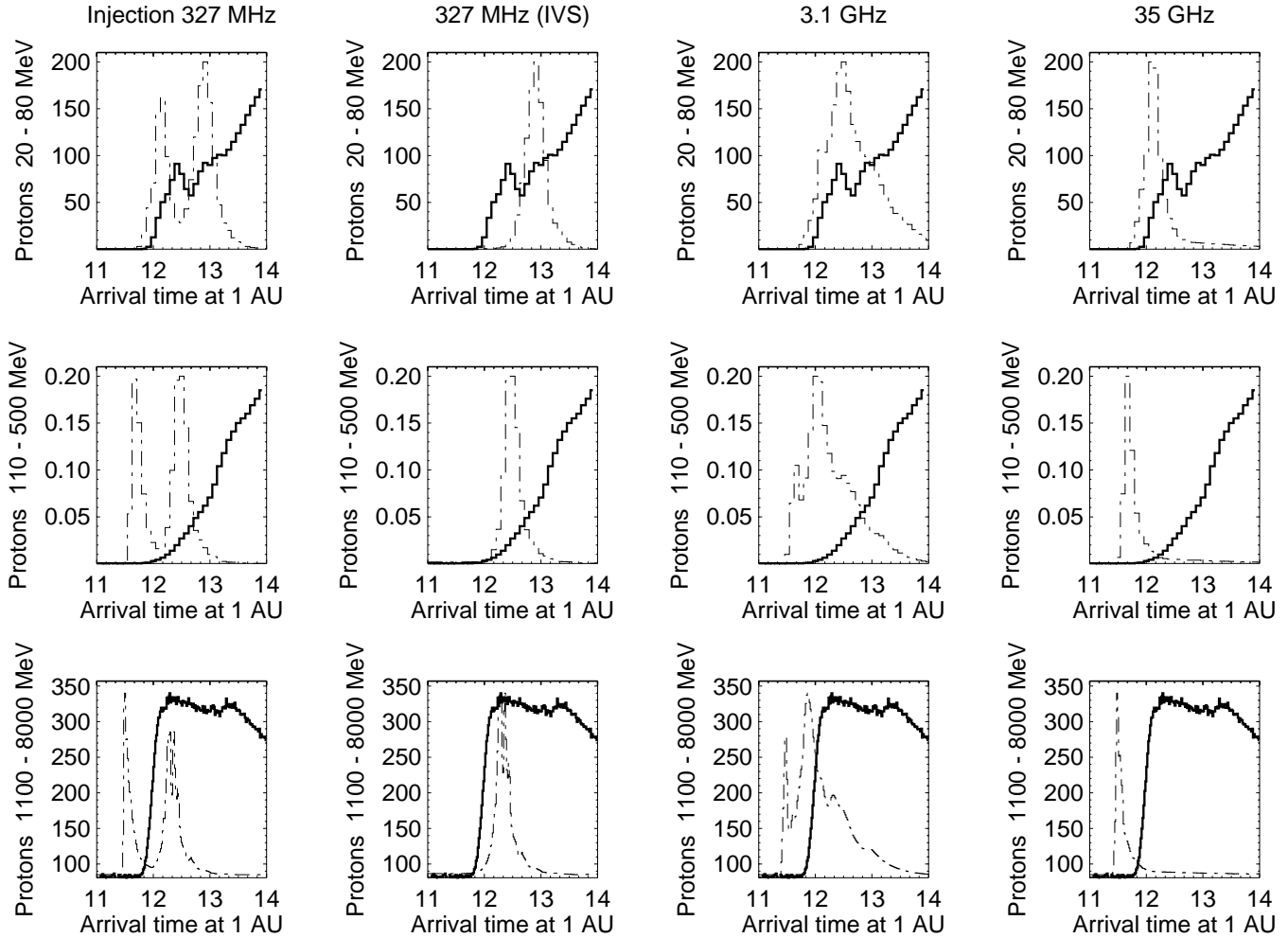


Fig. 9. Time histories of energetic proton count rates on 1989 September 29 at 1 AU (solid lines) and predicted time histories from a free-streaming model using radio time profiles as the tracer of the injection (dashed lines; cf. Sect. 4.3). Particle energy increases from the top to the bottom panel: 20–80 MeV (IMP-8), 110–500 MeV (GOES) and >1 GeV (Hobart neutron monitor; the high-energy cutoff at 8 GeV has been introduced for computational convenience). The integration time is 5 min for the spaceborne detectors, 1 min for the neutron monitor. The normalization of the computed time profiles is arbitrary and independent for the three energy ranges. The four columns differ by the time profile of the injection function used, as indicated at the top of the figure. In the second column only the stationary type IV continuum is used as injection function.

increase displayed by the GOES and neutron monitor observations is consistent with a source above the flaring active region slightly east of central meridian (cf. Fig. 6f). The analysis of neutron monitor measurements shows that the proton spectrum is harder during the gradual rise (Bieber & Evenson 1991; Shea et al. 1991; Stoker et al. 1995). At high energies the proton flux reaches a plateau near 15 UT, in conjunction with a new intense burst at dm-waves (e.g. 435 MHz, Fig. 10) whose source also seems to be above the flaring active region. The relativistic particle event starts to fade at 1530 UT.

4.5. Summary of observational results

The above results support the idea that particle injection in the low and middle corona contributes to the ≥ 20 MeV proton fluxes detected by the satellites and neutron monitors:

1. New rises of the time profile at 1 AU, when due to protons arriving from the Sun, have counterparts in signatures of new acceleration in the middle corona. Responses to acceleration during the main phase of the events in the whole radio band and to late acceleration processes visible predominantly at lower radio frequencies can be distinguished in the SEP and GLE profiles at 1 AU. The late particle injection produces relatively more high-energy protons at 1 AU than the injection during the main high-frequency radio emission. Most remarkably, during the 1989 September 29 event the most prominent high-frequency emission, which comes from a source region in the low corona, is not associated with relativistic protons.
2. The different rise times of the two components of the October 19 particle event can be well understood if particles are injected both near the flaring active region and in a remote source close to the well-connected interplanetary field line.

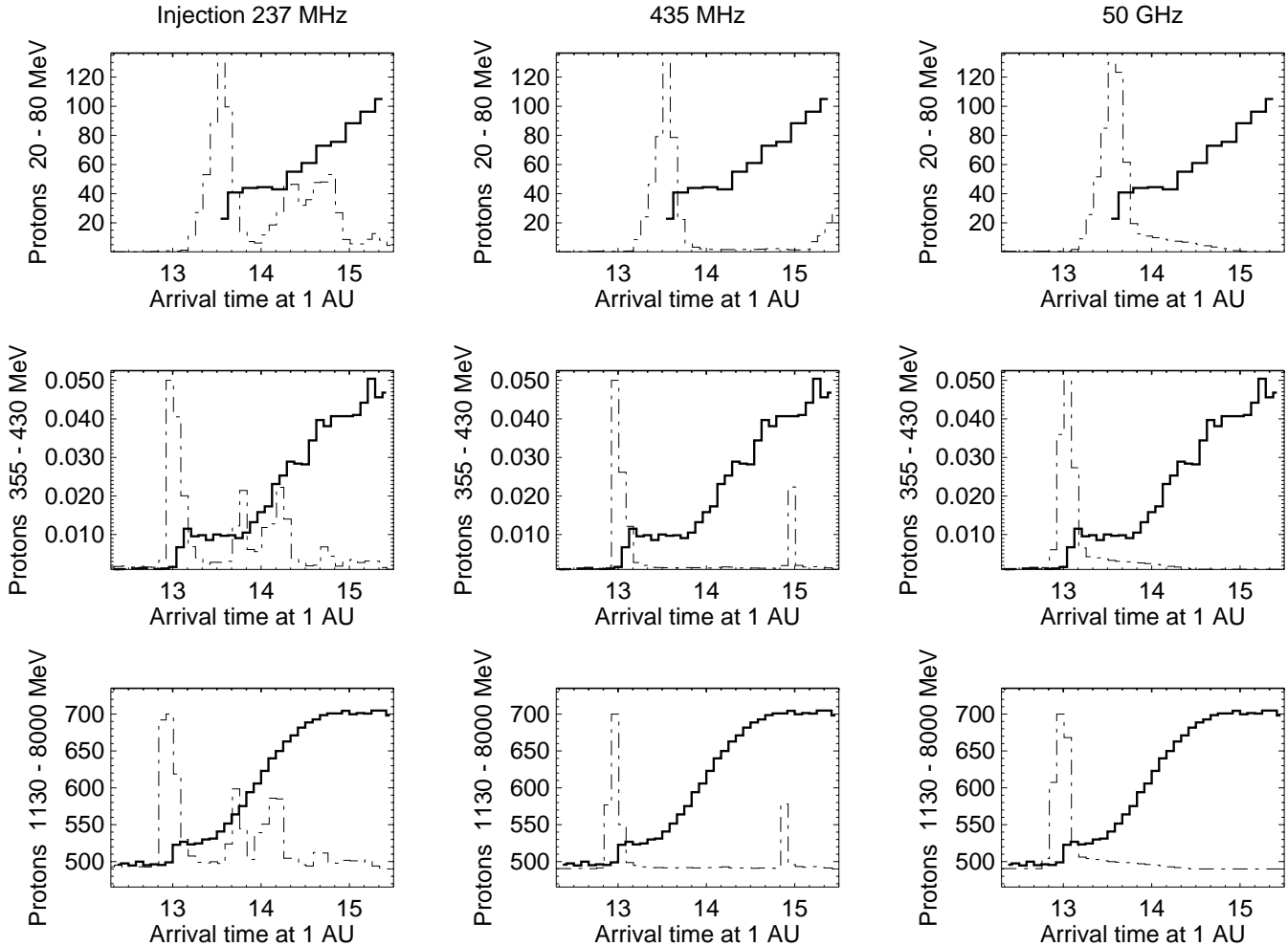


Fig. 10. Time histories of energetic protons observed on 1989 October 19 at 1 AU (solid lines) and predicted time histories from a free-streaming model using radio time profiles as the tracer of the injection (dashed lines). Data are from IMP-8 (20–80 MeV; observing gap 1148–1327 UT), GOES-HEPAD (355–430 MeV) and the Deep River neutron monitor. Cf. Fig. 9.

Radio sources are observed at both sites, and the $H\alpha$ event that extends over a large range of longitudes near central meridian comprises also a weak brightening in the western hemisphere.

5. Discussion

The correspondence observed during the two large SEPs of the present paper between successive episodes of coronal acceleration and new rises of the flux of protons above 20 MeV at 1 AU, and the different proton spectra associated with different rises, argue for a common acceleration process of interacting electrons and interplanetary protons during at least the first hours of the studied SEPs. If this occurred at the bow shock of a CME, the interacting particles would have to stream sunward from the extended shock front. The morphologies of soft and hard X-ray and radio sources which are all structured on much smaller scale than the angular span of the CME are inconsistent with this idea (cf. e.g. Kahler 1984; Klimchuk 1996, and references therein). In the events discussed by Kallenrode & Wibberenz (1991) this scenario is explicitly contradicted by the observation of elec-

trons that stream away from the Sun, emitting type III bursts at 2 MHz, i.e. at a height of about $10 R_{\odot}$ above the photosphere. Consequently, the present observations reveal that at least a significant fraction of the particles detected at 1 AU during the first hours of the gradual SEPs is supplied by acceleration processes at coronal heights less than $1 R_{\odot}$ above the photosphere, while the CME has travelled out to $10\text{--}20 R_{\odot}$.

Although we have studied only two events, the results do not stand alone. In the comparative study of a few events using *Helios* particle observations and ground-based radio data the ratio of proton to electron numbers was found to increase during a second rise of electromagnetic emissions from electrons in the low corona, whereas the impulsive phase produced no or weak proton injection (Bieber et al. 1980; Kallenrode & Wibberenz 1991). Proton richness is a typical feature of gradual SEPs, yet it appears related in time with a distinctly new injection of particles in the corona. During two large events in June 1991, Struminsky et al. (1994) and Akimov et al. (1996) showed proton or neutron spectra in conjunction with late radio emission to be harder than those associated with the impulsive phase.

The observations cannot exclude that the bow shock of the CME also contributes to the acceleration in the energy range discussed here. However, if, as we suggest, particles from the low and middle corona reach 1 AU during the first hours of the SEP, they must have travelled through the bow shock of the CME. This implies a low level of turbulence at frequencies at resonance with protons above 20 MeV. This means that diffusive acceleration is inefficient at the high energies that we consider. Late in the event, one expects to see particles carried along with the shock or with a flux rope, or trapped behind the shock (cf. Tylka et al. 1996; Reames et al. 1996). In situ measurements of shock-associated particles at that time are not relevant to the origin of the SEP as such, but to interplanetary propagation and acceleration which are well-known facts, especially at moderate energies (cf. Kallenrode 1993).

The action of an acceleration process at heights below $\sim 1 R_{\odot}$ is consistent with observations that were hitherto believed to favour the CME's bow shock:

1. The association of efficient proton injection into interplanetary space with *low-frequency* radio emission after the main microwave event is consistent with gradual SEPs being accelerated at greater altitudes than interacting particles observed during impulsive flares (cf. also Akimov et al. 1996). If the electrons yielding the late radio emission are accelerated in the vicinity of the radio source, the ambient density is of order $10^8\text{--}10^9\text{ cm}^{-3}$, provided the decimetric-to-metric emission is emitted near the local electron plasma frequency. Relativistic protons escaping from this region would have the required low ionization states, for which the product of the ambient electron density n_e and the residence time t must satisfy $n_e t < 3 \cdot 10^9\text{ cm}^{-3} \cdot \text{s}$ (Ruffolo 1997). The charge state peculiarities of gradual SEPs are then in the first place a question of where, not how, the acceleration occurs. Acceleration in the vicinity of the radio sources is also consistent with coronal abundances observed during gradual SEPs.
2. There are several reasons why a CME may be crucial for particle events, even if its bow shock is not the main accelerator at high energies: first, the CME on its way through the corona may trigger the release of energy stored in the magnetic fields of remote active regions. This would explain particle acceleration in the active region in the western solar hemisphere on October 19, implying a propagation speed $(1\text{--}2) \cdot 10^3\text{ km s}^{-1}$ if the CME starts at or before the onset of the main microwave emission. Second, the CME likely opens closed magnetic flux in various regions of the corona, thereby creating the conditions for post-eruptive energy release as discussed by Kahler & Hundhausen (1992), Hiei et al. (1993), Akimov et al. (1996) and Simnett et al. (1997), or for fast particle transport to field lines that were initially poorly connected with the acceleration site (e.g. Manoharan et al. 1996). Third, the CME leaves a turbulent plasma behind, and thus provides the ingredients for cross-field transport and pitch angle scattering of particles travelling through the perturbed plasma after acceleration at lower heights, and

for a prolonged duration of the proton flux enhancement at 1 AU.

None of these possibilities is inconsistent with a statistical correlation of one of the parameters characterizing the importance of CMEs, like speed or width, with the proton flux at 1 AU as reported by Kahler et al. (1984). But the argument that the correlation with speed is the key to understand the physical relationship between CMEs and gradual SEPs leaves a few questions unanswered: Why is there a weak statistical evidence that steeper proton spectra are associated with faster (and wider) CMEs (Kahler et al. 1984), rather than clear evidence of the contrary? Why does the correlation between CME speed and proton peak flux become much weaker when only CMEs with speeds $>800\text{ km s}^{-1}$ are considered (Kahler et al. 1987)? The intrinsic difficulty to infer a realistic speed of a three-dimensional CME from its limb-projected white-light signature certainly blurs the physical relationships. But altogether the available evidence for the speed correlation appears sufficiently ambiguous to the present authors to stimulate the search for alternatives to the scenario of bow shock acceleration.

The two large events discussed here confirm that flares are complex in space and time. Not all flares show the same degree of complexity, and not all comprise the long duration acceleration, but flares followed by gradual SEPs usually do. Scenarios which postulate that a flare is a point-like event in space and time have to give much weight to processes such as propagation effects, particle storage or bow shock acceleration at a CME. It is only when the temporal and spatial evolution of the flaring active region and its environment are considered that the effects of these processes in the high corona and the interplanetary space on SEPs can be understood.

Acknowledgements. The authors are indebted to the colleagues and institutions who generously made their data available: J. Burkepile, I. Garczynska & B. Rimpolt, L. Gentile and the PIs of neutron monitors, R. McGuire, Z. Mouradian & I. Soru-Escout, D. Neidig, M. Poquérusse, H. Sauer & D. Wilkinson (NOAA), A. Schroll and the late H. Urbarz. We thank R. Ramaty for providing calculations of gamma-ray spectra. We gratefully acknowledge discussions with M. Dryer, E. Flückiger, F.B. McDonald, D. Ruffolo, R. Vainio and N. Vilmer, as well as critical comments of the referees. One of us (ELC) wishes to acknowledge the support of Centre National de la Recherche Scientifique (CNRS), the Paris Meudon Observatory, the Alexander von Humboldt Foundation and a NATO Collaborative Research Fellowship which made his work possible. The use of the facilities and support of ELC by the Max-Planck-Institut für Extraterrestrische Physik, under Drs. G. Haerendel and J. Trümper, is greatly appreciated. The work at UNH was partially supported by NASA. We also appreciate the contributions of the late Mary M. Chupp in the analysis of the SMM GRS data and in the preparation of several early drafts of this manuscript.

Appendix A: SMM GRS observations

A.1. Response of the high-energy monitor to neutrons

Monte Carlo calculations for the GRS/HEM (Cooper et al. 1985) demonstrate that high energy neutrons characteristically deposit their energy predominantly in either of the separate CsI or NaI

elements of the GRS as compared to gamma-rays which shower, giving simultaneous energy loss in both GRS high-energy elements. A decreased ratio of “mixed” to “singles” counts therefore indicates an increased relative contribution of <500 MeV neutrons to the count rate. In the September 29 (October 19) event this ratio falls from an initial value of 0.16 (0.25) to less than 0.1 (<0.1).

A.2. Ratio of photon fluxes

in the ranges (1.1–1.8) MeV and (4.1–7.6) MeV

The fluences in these energy ranges include narrow line emissions from the deexcitation of the ambient target nuclei and Doppler-broadened line emissions from the accelerated interacting ions. Thus the ratio of the photon fluxes, R , depends on target density and composition and on the spectral shape and composition of the interacting particles. It can be used to distinguish thin target and thick target interaction regions (Trottet et al. 1996; Ramaty et al. 1997).

During the decay phase of the September 29 (October 19) flare R has an average value of 1.3 (1.2) and varies progressively from about ~ 1.4 (1.5) to ~ 1.1 (0.9). Such low ratios are not consistent with any reasonable values of thin target composition and accelerated particle composition, because they lead to extremely hard particle spectra, with negative slopes $s < 2$, which are inconsistent with the particle spectra ($3 \leq s \leq 5$) obtained from gamma-ray line analyses of other events (e.g. Ramaty et al. 1995, 1996; Share & Murphy 1995). On the other hand, the range of R observed is fully consistent with a thick target interaction region with composition C1 and accelerated particle composition II, with a power law spectrum with negative slope $s \sim 3.5$ flattening to $s \sim 2$ (Ramaty et al. 1997; Ramaty 1998, pers. comm.). C1 refers to an ambient particle composition based on SEP derived coronal composition and II refers to the accelerated particle composition of impulsive flares with average heavy element enhancements, both from Reames (1995). The similarity of values and evolution of R during the September 29 limb event and the October 19 disk flare, where thick target interaction is inevitable, emphasizes the thick target contribution to the September 29 event.

Appendix B: free-streaming distribution function

The distribution function $f(z, v, t)$ of freely streaming protons (z is the co-ordinate measured along the field line, v the particle speed, t the time of observation) obeys the equation

$$\frac{\partial f}{\partial t} + v \frac{\partial f}{\partial z} = q(z, v, t). \quad (\text{B1})$$

The injection function $q(z, v, t)dv$ gives the number of particles injected per unit time in the range $[v, v + dv]$ of speeds along the magnetic field line. The general solution to a similar transport equation has been given by Melrose & Brown (1976) and is used here changing their energy coordinate to the position coordinate z :

$$f(z, v, t) = \frac{1}{v} \int_{-\infty}^z dz' q(z', v, t - \frac{z - z'}{v}). \quad (\text{B2})$$

The start of the particle injection is at $t = 0$. We evaluate this expression assuming that space, speed and time can be separated in the injection function. A power-law in energy is assumed to describe the energy-dependent part of the injection function. Its spectral index δ is kept constant during the event. We further assume that protons are injected at a given point, z_0 , with a time profile identical to the flux density time history, $h(t)$, at a given radio frequency. The instantaneous energy spectrum of the protons as observed at $z > z_0$ is then

$$N(z, E, t) \sim E^{-(\delta + \frac{1}{2})} h(t - \frac{z - z_0}{v(E)}). \quad (\text{B3})$$

References

- Akimov V.V., Ambrož P., Belov A.V., et al., 1996, *Solar Phys.* 166, 107
- Anttila A., Kocharov L.G., Torsti J., Vainio R., 1998, *Ann. Geophys.* 16, 921
- Barat C., Trottet G., Vilmer N., et al., 1994, *ApJ* 425, L109
- Belian R.D., Gisler G.R., Clayton T., Christensen R., 1992, *JGR* 97, 16897
- Bhatnagar A., Jain R.M., Burkepille J.T., et al., 1996, *Ap&SS* 243, 209
- Bieber J.W., Earl J.A., Green G., et al., 1980, *JGR* 85, 2313
- Bieber J.W., Evenson P., 1991, *Proc. 22nd ICRC* vol. 3, 129
- Bruggmann G., Vilmer N., Klein K.-L., Kane S.R., 1994, *Solar Phys.* 149, 171
- Burkepille J.T., St.Cyr O.C., 1993, *NCAR Technical Note NCAR/TN-369+STR*
- Chupp E.L., 1996, in: Ramaty R., Mandzhavidze N., Hua X.-M. (eds.) *High Energy Solar Physics. AIP Conf. Proc.* 374, 3
- Chupp E.L., Trottet G., Marschhäuser H., et al., 1993, *A&A* 275, 602
- Cliver E., Kahler S., 1991, *ApJ* 366, L91
- Cliver E.W., Forrest D.J., Cane H.V., et al., 1989, *ApJ* 343, 953
- Cliver E.W., Feynman J., Garrett H.B., 1990, *JGR* 95, 17103
- Cooper J.F., Reppin C., Forrest D.J., et al., 1985, *Proc. 19th ICRC* vol. 5, 474
- Croom D.L., 1979, Jan. 1, *Solar Flare Millimeter Data*, Appleton Laboratory, Ditton Park, Slough, England
- Debrunner H., Lockwood J.A., Barat C., et al., 1997, *ApJ* 479, 997
- de Koning C.A., Bland C.J., 1995, *Proc. 24th ICRC* vol. 4, 212
- de Koning C.A., Mathews T., 1995, *Proc. 24th ICRC* vol. 4, 216
- Duldig M.L., Cramp J.L., Humble J.E., et al., 1993, *PASA* 10, 211
- Forrest D.J., Chupp E.L., Ryan J.M., et al., 1980, *Solar Phys.* 65, 15
- Hiei E., Hundhausen A.J., Sime D.G., 1993, *GRL* 20, 2785
- Kahler S.W., 1984, *Sol. Phys.* 90, 133
- Kahler S.W., 1992, *ARA&A* 30, 113
- Kahler S.W., 1994, *ApJ* 428, 837
- Kahler S.W., 1996, In: Ramaty R., Mandzhavidze N., Hua X.-M. (eds.) *High Energy Solar Physics. AIP Conf. Proc.* 374, 61
- Kahler S.W., Hundhausen A.J., 1992, *JGR* 97, 1619
- Kahler S.W., Sheeley N.R., Howard R.A., et al., 1984, *JGR* 89, 9683
- Kahler S.W., Cliver E.W., Cane H.V., et al., 1987, *Proc. 20th ICRC* vol. 3, 121
- Kai K., Nakajima H., Kosugi T., et al., 1986, *Sol. Phys.* 105, 383
- Kallenrode M.-B., 1993, *Adv. Space Res.* 13(9), 341
- Kallenrode M.-B., Wibberenz G., 1991, *ApJ* 376, 787
- Kanbach G., Bertsch D.L., Fichtel C.E., et al., 1993, *A&AS* 97, 349
- Kane S.R., McTiernan J.M., Loran J., et al., 1992, *ApJ* 390, 687
- Klein K.-L., 1987, *A&A* 183, 341

- Klein K.-L., Trottet G., 1994, In: Ryan J.M., Vestrand W.T. (eds.) High-Energy Solar Phenomena—A New Era of Spacecraft Measurements. AIP Conf. Proceedings 294, 187
- Klein L., Anderson K.A., Pick M., et al., 1983, Solar Phys. 84, 295
- Klein K.-L., Trottet G., Benz A.O., Kane S.R., 1988, In: Plasma Astrophysics. ESA SP-285, 157
- Klein K.-L., Aurass H., Soru-Escaut I., Kálmán B., 1997, A&A 320, 612 *Erratum* with correctly printed figures: A&A 322, 1027
- Klimchuk J.A., 1996, In: Bentley R.D., Mariska J.T. (eds.) Magnetic Reconnection in the Solar Atmosphere. ASP Conf. Series 111, 319
- Kocharov L.G., Kovaltsov G.A., Kocharov G.E., et al., 1994, Solar Phys. 150, 267
- Krucker S., Aschwanden M.J., Bastian T.S., Benz A.O., 1995, A&A 302, 551
- Kunow H., Wibberenz G., Green G., Müller-Mellin R., Kallenrode M.-B., 1991, In: Schwenn R., Marsch E. (eds.) Physics of the Inner Heliosphere. Vol. II, Springer, Berlin, p. 243
- Lario D., Sanahuja B., Heras A.M., 1998, ApJ 509, 415
- Leikov N.G., Akimov V.V., Volzhenskaya V.A., et al., 1993, A&AS 97, 345
- Lin R.P., 1985, Solar Phys. 100, 537
- Lin R.P., 1997, In: Trottet G. (ed.) Coronal Physics from Radio and Space Observations. Springer, Lecture Notes in Physics 483, 93
- Maia D., Vourlidis A., Pick M., et al., 1999, JGR 104, 12507
- Manoharan P.K., van Driel-Gesztelyi L., Pick M., Démoulin P., 1996, ApJ 468, L73
- Melrose D.B., Brown J.C., 1976, MNRAS 176, 15
- Miller J.A., Cargill P.J., Emslie A.G., et al., 1997, JGR 102, 14631
- Mirochnichenko L.I., Sorokin M.O., de Koning C.A., 1997, Proc. 25th ICRC vol. 1, 165
- Murphy R.J., Ramaty R., Kozlovsky B., Reames D.B., 1991, ApJ 371, 793
- Nakajima H., Dennis B.R., Hoynig P., et al., 1985, ApJ 288, 806
- Pick M., 1986, Solar Phys. 104, 19
- Radioheliograph Group, 1989, Sol. Physics 120, 193
- Ramaty R., Mandzhavidze N., Kozlovsky B., Skibo J.G., 1993, Adv. Space Res. 13(9), 275
- Ramaty R., Mandzhavidze N., Kozlovsky B., Murphy R.G., 1995, ApJ 455, L193
- Ramaty R., Mandzhavidze N., Kozlovsky B., 1996, In: Ramaty R., Mandzhavidze N., Hua X.-M. (eds.) High Energy Solar Physics. AIP Conf. Proc. 374, 172
- Ramaty R., Mandzhavidze N., Barat C., Trottet G., 1997, ApJ 479, 458
- Reames D.V., 1990, ApJ 358, L63
- Reames D.V., 1994, In: Solar Dynamic Phenomena and Solar Wind Consequences. ESA SP-373, 107
- Reames D.V., 1995, Adv. Space Res. 15(7), 41
- Reames D.V., Barbier L.M., Ng C.K., 1996, ApJ 466, 473
- Reeves G.D., Cayton T.E., Gary S.P., Belian R.D., 1992, JGR 97, 6219
- Ruffolo D., 1997, ApJ 481, L119
- Ruffolo D., Khumlumert T., Youngde W., 1998, JGR 103, 20591
- Sarris E.T., Krimigis S.M., 1985, ApJ 298, 676
- Share G.H., Murphy R.G., 1995, ApJ 452, 933
- Shea M.A., Smart D.F., Wilson M.D., Flückiger E.O., 1991, GRL 18, 829
- Simnett G.M., Tappin S.J., Plunkett S.P., et al., 1997, Solar Phys. 175, 685
- Smart D.F., Shea M.A., Wilson M.D., Gentile L.C., 1991, Proc. 22nd ICRC vol. 3, 97
- Stoker P.H., 1994, Space Sci. Rev. 73, 327
- Stoker P.H., Bieber J.W., Evenson P., 1995, Proc. 24th ICRC 24, vol. 4, 224
- Struminsky A., Matsuoka M., Takahashi K., 1994, ApJ 429, 400
- Swinson D.B., Shea M.A., 1990, GRL 17, 1073
- Torsti J., Vainio R., Anttila A., 1994, In: Solar dynamic phenomena and solar wind consequences. ESA SP-373, 263
- Trottet G., 1986, Solar Phys. 104, 145
- Trottet G., Chupp E.L., Marschhäuser H., et al., 1994, A&A 288, 647
- Trottet G., Barat C., Ramaty R., et al., 1996, In: Ramaty R., Mandzhavidze N., Hua X.-M. (eds.) High Energy Solar Physics. AIP Conf. Proc. 374, 153
- Tylka A.J., Boberg P.R., Adams J.H., et al., 1995, ApJ 444, L109
- Tylka A. J., Boberg P.R., Adams J. H., et al., 1996, In: Ramaty R., Mandzhavidze N., Hua X.-M. (eds.) High Energy Solar Physics. AIP Conf. Proc. 374, 96
- Tylka A.J., Dietrich W.F., Boberg P.R., 1997, Proc. 25th ICRC vol. 1, 101
- Vestrand W.T., Forrest D.J., 1993, ApJ 409, L69
- Vestrand W.T., Forrest D.J., 1994, In: Ryan J.M., Vestrand W.T. (eds.) High-Energy Solar Phenomena—A New Era of Spacecraft Measurements. AIP Conf. Proceedings 294, 143
- Vilmer N., Trottet G., Barat C., et al., 1999, A&A 342, 575